



Submeso Motions and Intermittent Turbulence Across a Nocturnal Low-Level Jet: A Self-Organized Criticality Analogy

Daniela Cava¹ · Luca Mortarini^{1,2} · Umberto Giostra³ · Otavio Acevedo² · Gabriel Katul^{4,5}

Received: 30 June 2018 / Accepted: 5 March 2019
© Springer Nature B.V. 2019

Abstract

One of the hallmarks of the stable boundary layer is the switching between turbulent (active) and non-turbulent (passive) states. In very stable conditions, the boundary layer becomes layered with fully-developed turbulence confined to a shallow region near the surface. In the quiescent region above this near-surface layer, the turbulence is weak, intermittent and detached from the ground. These conditions promote the development of a low-level jet that re-energizes the turbulence through an elevated shear layer. The Monin–Obukhov similarity theory fails in the layered stable boundary layer thereby making the quantification of mixing and transport properties challenging for numerical models. In the present study, multi-level time series from a tall (140 m) meteorological tower are analyzed using the telegraphic approximation to investigate analogies with a general class of intermittency models that include self-organized criticality. The analogy between turbulence and self-organized criticality is restricted to clustering properties of sign changes of flow variables for describing switching between turbulent and non-turbulent states. The telegraphic approximation provides a new perspective on clustering and on external and internal intermittency for periods dominated by turbulent motions, a low-level jet and submeso motions. Some of these periods are characterized by the absence of turbulence but occasionally punctuated by bursts of intermittent turbulent events. The switching probability of active–inactive states and the lifetimes of inactive states (related to intermittent turbulent bursts) show evidence of self-organized-criticality like behaviour in terms of scaling laws. The coexistence of self-organized criticality and intermittent turbulence may offer new perspectives on the genesis of scaling laws and similarity arguments, thereby improving the performance of numerical models in the stable boundary layer.

Keywords Intermittent turbulence · Low-level jet · Self-organized criticality · Stable boundary layer · Submeso motions

Electronic supplementary material The online version of this article (<https://doi.org/10.1007/s10546-019-00441-8>) contains supplementary material, which is available to authorized users.

✉ Daniela Cava
d.cava@isac.cnr.it

Extended author information available on the last page of the article

1 Introduction

While the significance of stable boundary-layer (SBL) flows in transporting heat, moisture, and contaminant is not in dispute, characterizing SBL dynamics continues to draw inquiry and research attention. For mildly stable conditions, where the Richardson number $Ri \ll 0.25$, the flow statistics scale reasonably with Monin–Obukhov similarity theory (Mahrt 1998; Pahlow et al. 2001; Grachev et al. 2005). Here, $Ri = (\beta)(\partial\theta/\partial z)(S)^{-2}$ is a non-dimensional parameter that measures the ratio of buoyancy destruction (in the SBL) to the mechanical production of turbulent kinetic energy (TKE), where $\beta = g/\theta$ is the buoyancy parameter, g is the acceleration due to gravity, $S = d\bar{u}/dz$ is the mean velocity gradient, \bar{u} is the mean horizontal wind speed, and θ is the mean potential temperature. With increasing stability, Ri becomes large, the SBL becomes layered (especially when $Ri \gg 0.25$), and fully-developed turbulence may be confined to shallow regions near the ground where the mechanical production term (S) remains locally large. Away from this confined region, a quiescent layer in which turbulence is weak or intermittent develops, conducive to the formation of a low-level jet (LLJ) and the propagation of submeso motions (Banta et al. 2007; Mortarini et al. 2018). Accompanying the LLJ is the intermittent production of TKE at an elevated source from the ground roughly located at the nose of the jet (where \bar{u} is maximum). The layering within the SBL poses challenges in quantifying mixing and transport properties, especially in numerical weather prediction. In the quiescent region, the significant role of fine-scale turbulent eddies, external intermittency or bursts in turbulence, and the fact that eddies become detached from the ground at finite distances from the surface introduce major departures from the widely used Monin–Obukhov similarity theory (Mahrt 2014; Acevedo et al. 2015; Monahan et al. 2015; Lan et al. 2018). Moreover, the anisotropy in the energetics of eddies becomes accentuated when $Ri \gg 0.25$ compared to near-neutral or slightly stable conditions ($Ri \ll 0.25$). This anisotropy results from the strong damping of vertical turbulent motions by buoyancy forces whereas the horizontal motions remain finite and occasionally large because of the straining action due to shear forcing (Smyth and Moum 2000). Energetically, eddies become disk-like and this shape describes integral lengths of eddies in all three directions. The pressure redistribution or ‘return-to-isotropy’ term is unable to support the efficient redistribution of energy between the horizontal (where the TKE production term is introduced) and vertical directions because buoyancy (responsible for the TKE destruction) is sufficiently large and the associated relaxation time scale of the return-to-isotropy becomes small (Bou-Zeid et al. 2018). These conditions lead to one of the defining hallmarks of the SBL, i.e., the switching between turbulent (active) and non-turbulent (passive) states. The anisotropy of turbulence and the consequences of switching between active and inactive states to intermittent turbulent transport of heat and momentum continue to pose barriers to progress within numerical weather prediction (Stiperski and Calaf 2018; Vercauteren et al. 2018). The work proposed here does not claim to address this challenge. However, identifying connections between such SBL states and a general class of intermittency models describing on–off and off–on switching may offer a logical starting point (Bershadskii et al. 2004; Sreenivasan and Bershadskii 2006). In particular, we ask whether self-organized criticality (SOC) is a plausible intermittency model for such on–off and off–on switching thereby offering a new perspective on the genesis of scaling laws and similarity arguments in the very stable SBL. The analogy between turbulence and SOC has been recently confirmed in direct numerical simulations of strongly stratified mixing layers where turbulence is generated by the so-called Holmboe wave (Salehipour et al. 2018). This analogy motivated

the data analysis undertaken here. Self-organized criticality is associated with dissipative systems possessing many degrees of freedom that operate near a configuration of minimal stability or critical configuration (Sornette 2003; Pruessner 2012). In such a state, small disturbances can cause events of all sizes (or durations) characterized by power-law distributions. The classical experiment motivating SOC is the well-studied sand-pile model where, in the long run, the sand-pile slope evolves to a critical state where an added single grain of sand is likely to just settle on the pile, but also has a non-negligible probability of triggering an avalanche. This experiment suggests that the critical state is sensitive to external stimuli because a small variation can cause a large response (Bak et al. 1988).

In terms of turbulent quantities, radiative cooling increases buoyancy destruction that squashes eddies in the vertical direction (both in size and turbulent kinetic energy). For very stable states, the pressure-redistribution (or return-to-isotropy) is inefficient in transferring kinetic energy from the planar components to the vertical. However, any disturbance to this regime allows some of the turbulent potential energy stored in the vicinity of the LLJ nose to be released into localized bursts of sensible heat flux, which then affect the generation of TKE in the vertical direction (Mortarini et al. 2018). Pressure redistribution becomes efficient and transfers this localized burst of energy in the vertical direction to the horizontal components. Such bursts in TKE are responsible for the formation of intermittent turbulence. The work here distinguishes between two types of intermittency: ‘external intermittency’ is used to characterize an intermittent turbulent state describing the velocity components themselves; ‘internal intermittency’ is presumed to be associated with corrections to Kolmogorov scaling (Kolmogorov 1941; hereinafter referred as K41) in the inertial subrange (ISR) as well as finer scales and is linked to velocity gradients rather than the velocity components. A localized turbulent burst disrupts and weakens the mean temperature gradient that has been established by radiative cooling allowing self-sustained TKE over durations longer than the burst duration itself. The switching probability of active-inactive states and the lifetimes of inactive states (related to intermittent turbulent bursts in the SBL) may show evidence of SOC-like behaviour in terms of scaling power laws.

To clarify this issue and explore some aspects of the analogy between SOC and the SBL, multi-level high frequency time series are analyzed from measurements taken on a tall (140 m) meteorological tower. The selected period includes three phases: a weakly stratified state at the beginning of the nocturnal period ($Ri \sim 0.1$), a transition period characterized by a higher stratification ($Ri \gg 0.25$), and a period in which the LLJ developed across the quiescent layer where Ri indicates a layered structure of the SBL, with fully-developed turbulence close to the ground ($Ri \sim 0.1$) and turbulence detached from the ground that is intermittently produced in the layer beneath the LLJ nose (Ri oscillating between 0.2 and 0.5). The focus is on scaling laws, event clustering, and connections between on–off and off–on switching as viewed from a SOC perspective with corrections introduced due to intermittent turbulence in all three phases and all three layers (near the ground, in the quiescent layer, and above the LLJ nose). Aspects of the submeso motions that develop after the formation of the LLJ are shown to carry signatures of the co-existence of SOC and intermittent turbulence, especially in event clustering and intermittency exponents within the quiescent layer. To be clear, this is not the first instance for which turbulence properties are found to share some resemblance to SOC (Sreenivasan et al. 2004) or that SOC and intermittent turbulence may coexist (symbiotically) (Uritsky et al. 2007). However, this may be the first instance where connections and the coexistence of SOC and intermittent turbulence in the SBL are analyzed prior to and after the formation of a LLJ using multi-level time series of wind velocity components and temperature. Here, the focus is on externally forced intermittency affecting the production scales of turbulence and

driven by non-stationary and localized shear produced by the LLJ and submeso motions (Mahrt 2014). Furthermore, internal or small-scale intermittency resulting from interaction between turbulence and the shear in the mean flow affecting the transfer and dissipation of TKE at smaller scales is investigated (Tennekes 1973; Sreenivasan and Antonia 1997).

2 Measurements

2.1 Experimental Set-Up

The study is based on the flow field measured during a nocturnal period at a coastal site in Espírito Santo State (10°31'53"S; 39°48'03"W), south-eastern Brazil. The tower is located in a continental area at a distance of 4 km from the coast in a region where the coastline of the Atlantic Ocean has a south-south-west to north-north-east orientation. The terrain is generally flat up to 30 km from the tower location. The wind velocity components (u , v , w) and air temperature (T) were collected at a sampling frequency of 10 Hz using 3-axis sonic anemometers (Campbell CSAT 3b) positioned at 11 levels (1, 2, 5, 9, 29, 37, 56, 75, 94, 113 and 132 m) above the surface. The 140-m tower instrumentation was designed to provide a detailed characterization of the vertical structure of the lowest portion of the atmospheric boundary layer. The tower has been installed directly to the north of the facilities of Linhares Geração SA, a thermoelectric power plant, at a distance of 245 m from the main buildings, which are 13.8 m high. Details about the experiment can be found in Acevedo et al. (2018) and Mortarini et al. (2018).

2.2 The Case Study

Data analyzed here have been sampled between 8 and 9 October 2016 from 2100 to 0500 local standard time (hereinafter LST). The selected night was characterized by a nocturnal breeze circulation associated with the absence of forcing at the synoptic scale that allowed the formation of a coastal LLJ. Figure 1 shows the averaged wind-speed profiles every 1 min and Fig. 2 shows the contour plot of the gradient Richardson number in finite difference form ($Ri = \beta \Delta \theta \Delta z \Delta \langle U \rangle^{-2}$) during the night, where $\Delta \theta$ is the potential temperature difference measured across a layer of thickness $\Delta z = z - z_{ref}$, z is the height above the ground and z_{ref} is a reference height (2 m in the present work), and $\Delta \langle U \rangle$ is the accompanying wind-speed difference at height z . The Ri value evaluated every minute at each height z was used as a measure of the atmospheric stability. This choice of this form of Richardson number is less vulnerable to measurement errors when compared to the flux Richardson numbers given the small fluxes and the non-monotonic mean wind-speed-profile shape in the very stable boundary layer.

Figures 1 and 2 highlight the transition of the mean wind-speed profile from a nearly logarithmic shape at the start of the evening (first phase, characterized by a weakly stable boundary layer, $Ri \sim 0.1$) to a short period of light winds at 2230 LST. This period was associated with the arrival of a cold airmass originating from land and subsiding as the airmass encountered coastal water. The influence of this event tended to progressively affect all measurement levels between 2230 and 0100 LST (second phase, characterized by high stability with $Ri \gg 0.25$). At 2300 LST, the activation of a jet commenced and became fully-developed at 0100 LST, reaching its final height of 56 m and its maximum speed of 4 m s^{-1} at 0300 LST. In the period between 0100 and 0500 LST, the SBL became layered

Fig. 1 Temporal evolution of the averaged wind-speed profiles evaluated every minute relative to the night between 8 and 9 October 2016

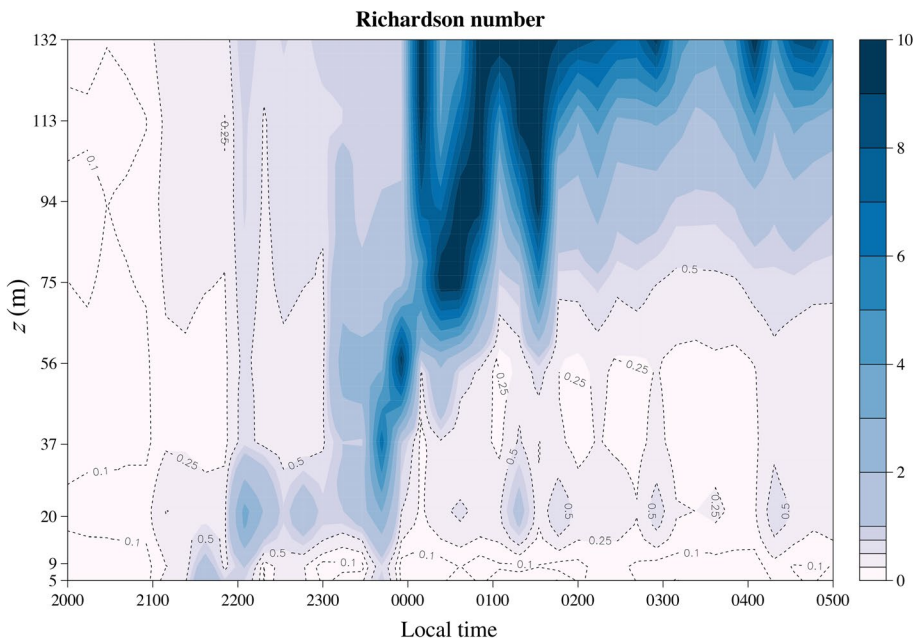
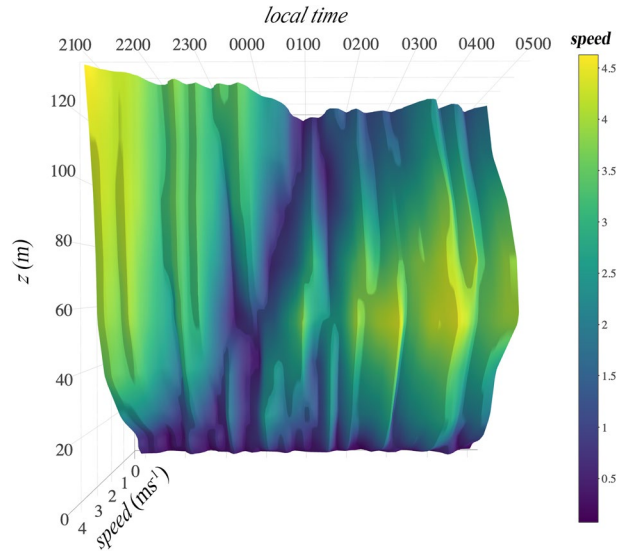


Fig. 2 Contour plot of the Richardson number evaluated every minute relative to the night between the 8 and 9 October 2016

with fully-developed turbulence confined to a shallow region near the ground (where $Ri \sim 0.1$) and a region immediately under the LLJ nose between the heights of 10 and 56 m where Ri assumed values ranging from 0.2 to 0.5, suggesting that the SBL is near a ‘phase transition’ between turbulent ($Ri < 0.25$) and non-turbulent states. The statistical properties

of the LLJ and layered structure of the SBL have been investigated and reported elsewhere (Mortarini et al. 2018) and are not repeated here. After the complete development of the LLJ (after 0100 LST, third phase), three distinct layers were identified: a thin stable boundary layer below 20 m, a quiescent layer close to the LLJ nose and a turbulent layer above 94 m. In the quiescent layer, the TKE and fluxes were very small, tending to increase close to the ground and intermittently in the turbulent layer above 94 m (see Fig. 9 in Mortarini et al. 2018). One of the main results from the aforementioned study was the observation of both horizontal and vertical submeso motions throughout the entire measurement domain after LLJ inception. The detected and persistent fluctuating horizontal velocity components were characterized by periods ranging between 16 and 50 min and were responsible for the apparent ‘pulsing’ of the LLJ nose, also evident in Fig. 1. On the other hand, vertical waves discontinuously activated in the quiescent layer propagate below and above it, with the waves disrupting and triggering intermittent turbulent events at the boundaries and outside the quiescent layer.

3 Method of Analysis

Clustering and intermittency properties of the flow variables before, during, and after the evolution of the LLJ were investigated by employing the telegraphic-approximation method. For completeness, the approach and the definition of various scaling exponents are briefly described. Further details are presented in Bershadskii et al. (2004) and Sreenivasan and Bershadskii (2006), hereafter referred to as B04 and SB06, respectively.

3.1 The Telegraphic Approximation

The telegraphic approximation (*TA*) of a zero-mean variable $s(t)$ was defined by B04 and SB06 as,

$$TA(s) = \frac{1}{2} \left(\frac{s'(t)}{|s'(t)|} + 1 \right) \quad (1)$$

where $s'(t) = s(t) - \bar{s}$ and the overbar indicates time averaging. Thresholds other than a zero-mean can be used, but here the definition in Eq. 1 was adopted throughout for consistency with prior studies (B04; SB06; Cava and Katul 2009; Poggi and Katul 2009; Cava et al. 2012). Figure S1 (in Online Resource 1) shows an example of a 30-min time series of the lateral velocity component (top) and the corresponding *TA* values (bottom). The telegraphic approximation preserves the so-called zero-crossing properties of the original series but removes amplitude variations. Thus, the binary nature (on–off) of the telegraphic approximation allows the isolation of clustering events at different time scales without being influenced by amplitude variations.

3.2 Spectra

The ‘switches’ from 0 to 1 or 1 to 0 in the *TA* series may be correlated in time if they are associated with coherent events (turbulent or not is irrelevant). Such a correlation structure can be investigated by considering the relation between the spectral scaling exponents of $s(t)$ (affected by both amplitude variability and clustering) and of $TA(s)$ (affected only by

the memory of the on–off or off–on switching). Denoting the spectra of $s'(t)$ as $E_s(f)$ and of its telegraphic approximation as $E_{TA}(f)$ (where f is the frequency) and assuming that these spectra scale as f^{-n} and f^{-m} , respectively, then the goal is to establish a relation between m and n . A number of experiments and analyses on a wide range of stochastic processes (including $1/f$ noise) already showed that the spectral exponents n and m are linearly related by

$$m = an + b. \quad (2)$$

SB06 heuristically obtained $a = b = 1/2$ for a wide range of stochastic processes, including turbulence far away from boundaries. Hence, for $n = 5/3$ (typical of ISR scaling in turbulent spectra), the expression of SB06 predicts $m = 4/3$. That is, the telegraphic approximation exhibits slower spectral energy decay with increased frequency when compared to the original series. Although the precise values of a and b differ among various studies including canopy sublayer and surface-layer turbulence (Cava and Katul 2009; Poggi and Katul 2009; Cava et al. 2012), the spectral decay in telegraphic approximation appears to be generally slower when compared to $s(t)$. Equation 2 also suggests that when $n < 1$, the spectral decay in telegraphic approximation becomes steeper than its $s(t)$ counterpart (i.e. more memory in the off–on and on–off switching than the original series as has been shown for rainfall by Molini et al. 2009). These experimental results suggests that amplitude variability may de-correlate the series relative to the memory in on–off or off–on switching.

3.3 Non-Gaussianity

An important property of the telegraphic-approximation technique is its capacity to partially preserve the non-Gaussian properties encoded in the intermittency of the original time series. In a turbulent field, intermittency and the resulting non-Gaussianity of turbulent velocity gradients is a consequence of the non-linear dynamics of the Navier–Stokes equations. As a matter of fact, one of the characteristics of inhomogeneous and intermittent turbulence is the non-zero skewness of the velocity and of the velocity gradient distributions. The telegraphic-approximation technique preserves the non-Gaussian properties of the original series using the fraction of time (Γ_+) describing the ‘on’ phases ($TA = 1$). In particular, the skewness of an arbitrary flow variable ($Sk_s = \langle \hat{s}^3 \rangle$; $\hat{s} = \frac{s'}{\sigma_s}$, where σ_s is the standard deviation of $s(t)$) can be analytically linked to Γ_+ using a third-order cumulant expansion method (CEM) of the probability density function (p.d.f.) (Nakagawa and Nezu 1977; Raupach 1981; Katul et al. 1997; Poggi et al. 2004; Katul et al. 2006) given as

$$p(\hat{s}) \approx \left[\left(\frac{1}{\sqrt{2\pi}} \right) \exp(-\hat{s}^2/2) \right] \left(1 + (1/6)Sk_s(\hat{s}^3 - 3\hat{s}) \right), \quad (3)$$

where the term in the squared bracket represents a Gaussian distribution and the term in the rounded bracket represents the first-order correction to a Gaussian distribution. The fraction of time $\hat{s} > 0$ ($= \Gamma_+$) can be derived via,

$$\Gamma_+ = \int_0^\infty p(\xi) d\xi = (1/2) - (1/12)Sk_s \sqrt{2/\pi}, \quad (4)$$

which can be used to assess how well the telegraphic approximation preserves non-Gaussianity in the original time series.

3.4 Clustering Exponents

Within the telegraphic-approximation framework, clustering is linked with the correlation in space or time of the on–off and off–on binary switches. SB06 determined the clustering exponent from scaling relations applied to the density of zero-crossing ($n_\tau(t)$). The time series of $n_\tau(t)$ was computed from the number of zero-crossings for the portion $s'(t)$ to $s'(t + \tau)$ normalized by the total number of points in the time interval τ and the clustering exponent (α) was determined by the following expression

$$\overline{\delta n_\tau^2}^{1/2} \sim \tau^{-\alpha}, \quad (5)$$

where $\delta n_\tau(t) = n_\tau(t) - \overline{n_\tau(t)}$, and $\overline{n_\tau(t)}$ is the long-term mean zero-crossing density. For white noise, taken here as an example of no significant clustering, $\alpha = 0.5$. On the other hand, for well-developed turbulence extrapolated to infinite Taylor microscale Reynolds number (Re_λ), SB06 demonstrated large clustering characterized by $\alpha = 0.1$. In the same study for a finite $Re_\lambda \in [200, 20000]$, α ranged from 0.25 to 0.40 within the ISR, but approached a white noise value (i.e. 0.5) at larger scales. This behaviour reflects the scale-independent near-Gaussian behaviour of the statistics of the velocity-difference amplitude at large scale (decorrelated in time), as well as the scale-dependent non-Gaussian statistics in the ISR observed in a number of studies (SB06; Katul 1994; Katul et al. 1994, 2009; Meneveau 1991; Sreenivasan and Antonia 1997, inter alia).

3.5 Intermittency Exponents

Because variance (or energy) dissipation rate is proportional to the squared spatial gradients, converted to temporal gradients using Taylor's frozen-turbulence hypothesis, the internal intermittency properties of a turbulent series at small scales can be inferred from the scaling of the moments (e.g. B04, SB06),

$$\frac{(\overline{\xi_\tau(t)})^q}{(\overline{\xi_\tau(t)})^q} \sim \tau^{-\mu_q} \quad (6)$$

where $\xi(t) = \left| \frac{ds(t)}{dt} \right|^2$ and $\xi_\tau = (1/\tau) \int_t^{t+\tau} \xi(t) dt$. The scaling exponents (μ_q) for differing $q(> 1)$ were first proposed as measures of small-scale intermittency by Obukhov (1962) and subsequently were used in turbulence research (Kuznetsov et al. 1991, 1992; Sreenivasan and Antonia 1997; Katul et al. 2001, 2009; Giostra et al. 2002; Shi et al. 2005). For comparison with previous studies (SB06; Cava and Katul 2009; Poggi and Katul 2009; Cava et al. 2012), the second-order exponent (μ_2) was computed for $s(t)$ and its telegraphic approximation. These two exponents are referred to as μ_s and μ_{TA} , respectively. Information on both amplitude and clustering of series are contained in μ_s , while a non-zero value of μ_{TA} indicates a clusterized distribution of pulses in the dissipation rate for $TA(s)$. As a consequence, $\mu_{TA} > \mu_s$ indicates that amplitude variations *mitigate* internal intermittency; $\mu_{TA} < \mu_s$ indicates that amplitude variations *amplify* internal intermittency; $\mu_{TA} \sim \mu_s$ indicates that the observed intermittency may be mainly due to clusterization and not to amplitude variations.

The study of SB06 demonstrated that μ_s (for $s = u$) linearly decreases with decreasing $1/\ln(Re_\lambda)$ and approaches 0 as $Re_\lambda \rightarrow \infty$. Moreover they found a linear correlation between clustering and intermittency exponents ($\mu_s(Re_\lambda) = \alpha(Re_\lambda) - 0.1$) that implies that clustering at fine scales explains all the variations in μ_s (affected by both clustering and amplitude variability) as Re_λ varies. Cava et al. (2012) found that such a relation holds across a wide range of stability and surface roughness conditions for the longitudinal velocity component and scalars, with the regression slope increasing with increasing surface roughness. On the other hand, a de-correlation between α and the intermittency exponents for the vertical velocity component was observed with progressively increasing smoothness of the surface. These results were used to suggest that surface roughness might affect the structure of fine-scale turbulence in the vertical direction within the ISR. Other evidence that surface roughness may affect ISR scaling has been reported elsewhere as well (Kuznetsov et al. 1992; Poggi et al. 2003; Katul et al. 2009).

3.6 Inter-pulse Periods and Linkages Between Various Exponents

A relation between durations of inter-pulse periods and temporal correlation of ‘on–off’ or ‘off–on’ switches is expected for a TA series. For a weighted superposition of Poisson processes, it was shown by Jensen (1998) that

$$m = 3 - \gamma \quad (7)$$

where γ is the exponent of the power-law distribution $p(I_p) \sim I_p^{-\gamma}$, $p(\cdot)$ is the p.d.f. of the distribution of inter-pulse periods $I_p(i) = \hat{t}_{i+1} - \hat{t}_i$, and \hat{t}_i is the time for which $TA(s(t_i))$ switches. Interestingly the same relation holds also for systems near critical behaviour (as may be expected from SOC). B04 proposed an ‘intermittency’ correction to Eq. 7 yielding

$$m = (3 - (\mu_s/2)) - \gamma. \quad (8)$$

and moreover, SB06 showed that turbulence may be classified as ‘active’ or ‘passive’ depending on the scaling laws of $p(I_p)$. In particular, for ‘active’ scalars $p(I_p) \sim I_p^{-\gamma}$, while for ‘passive’ scalars they found a log-normal distribution of the form

$$p(I_p) \sim \exp(a\theta^2 + b\theta + c), \quad (9)$$

where $\theta = \ln(I_p)$, a is related to the variance of θ , and b and c are related to the mean (β) and variance (σ^2) of θ , given by

$$a = -1/(2\sigma^2), \quad (10a)$$

$$b = -1 + 2\beta a, \quad (10b)$$

$$c = -\ln(\sqrt{2\pi}\sigma) - \beta^2 a. \quad (10c)$$

This finding is rather surprising because δ -correlated processes (i.e. white noise) exhibit a log-normal distribution of inter-pulses, while according to SB06, $p(I_p) \sim I_p^{-\gamma}$ results in an energy spectrum more consistent with the traditional Lorentzian form of processes with exponentially-distributed inter-arrival times. The term ‘active’ as used in SB06 refers to flow variables where the source strength determines the scalar dynamics, such as for temperature in convective turbulence, where the amount of heat injected determines the degree of convection. Cava et al. (2012) found that $p(I_p)$ was well approximated by a power-law distribution with an exponential cut-off for velocity and scalar concentration measurements

above a forested ecosystem. Moreover, power laws for the entire range of I_p above smoother surfaces for all flow variables (except w) was reported in the same study. However, when restricting I_p to events shorter than the integral time scale (i.e. to time scales comparable to those within the ISR), a power-law distribution ($p(I_p) \sim I_p^{-\gamma}$) emerged for all flow variables and stability classes (even for w). The power-law exponent γ appeared to be related to the telegraphic-approximation spectral exponent m via Eq. 7, indicating that telegraphic-approximation properties of atmospheric turbulence may share some resemblance to SOC.

4 Results

4.1 Spectral Properties of the Telegraphic Approximation for Flow Variables Across the Low-Level Jet

Spectral properties of the measured flow variables and their telegraphic approximation during the evolution of the LLJ are investigated. Examples of hourly spectral densities for the longitudinal and vertical velocity components and their telegraphic approximation before (2100 LST) and after (0300 LST) the development of the LLJ are shown in Figs. S2 and S3 (in Online Resource 1). The comparison of the spectra highlights an increment of energy in the low-frequency range when the LLJ develops (Fig. S3a, b), associated with both horizontal meandering oscillations and gravity waves, more pronounced in the quiescent layer (between 20 and 94 m-dashed lines). The low-frequency maxima associated with the sub-meso motions are visible also in the telegraphic-approximation spectra (Fig. S3c, d). This finding suggests that the tendency of these structures associated with the submeso motions is to be clustered in time (or space) and it is captured by the telegraphic-approximation spectra. Before the development of the LLJ (Fig. S2a, b), spectra at different measurement levels exhibit spectral decay ($n = 5/3$) predicted by K41 theory for locally homogeneous and isotropic turbulence at high Reynolds number in the ISR. After the LLJ development (Fig. S3a, b), spectra clearly diverge from K41 scaling in the quiescent layer, whereas K41 scaling was approximately observed close to the ground ($z < 20$ m) and in the turbulent layer above 94 m (i.e. regions where production of TKE is sustained).

The TA spectra exhibit a similar behaviour. In general, they confirm the slower spectral energy decay predicted by SB06 in the ISR ($m = 4/3$), but clearly diverged from this expectation in the quiescent layer after the LLJ development (Fig. S3c, d). This behaviour is also evident in Figs. 3 and 4, which show the profiles of the spectral exponents for all the measured variables and their telegraphic-approximation counterparts. The spectral exponents were computed in the frequency range between 0.1 Hz and 2 Hz, chosen as the ISR. This uniform frequency interval was selected for all the analyzed hours and heights to highlight deviations from K41 scaling at small scales in different cases. The lowest limit ($f = 0.1$ Hz) was chosen to minimize contamination from large scales; the highest limit ($f = 2$ Hz) was chosen to minimize white-noise distortions roughly exhibiting a flat spectrum for $f > 2$ Hz.

The deviation from K41 values for spectral exponents ($n = 5/3$ and $m = 4/3$, indicated by the vertical dotted lines in Figs. 3 and 4) is evident after 0100 LST and is more pronounced in the quiescent layer between 20 m and 94 m. This is true for all the wind-velocity components as well as air temperature.

The relation between the spectral exponents ($=n$) of 1-h runs and of their TA values ($=m$) for all the flow variables and for the period before (Fig. 5a) and after (Fig. 5b) the

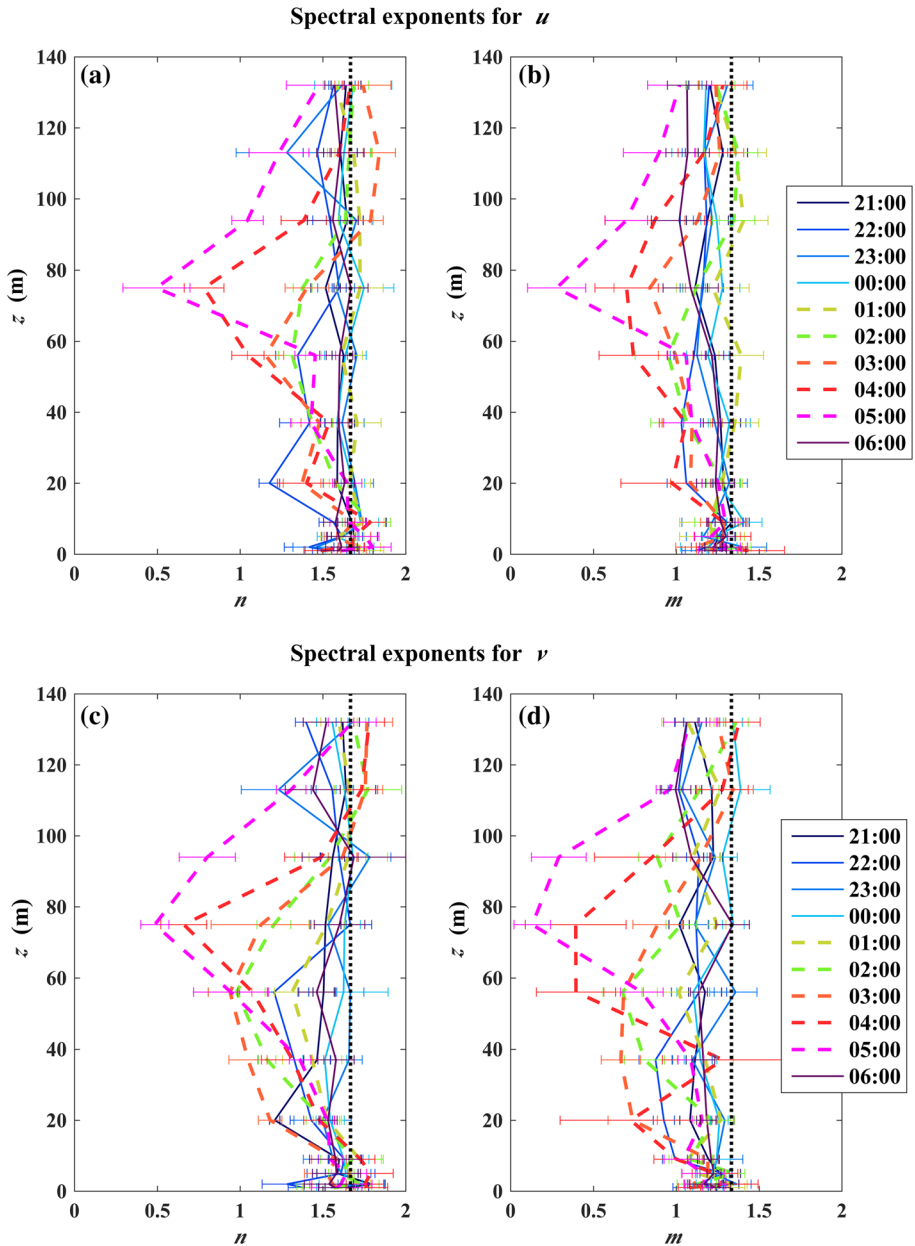


Fig. 3 Hourly vertical profiles of spectral exponents of the measured signals (n) and the correspondent telegraphic approximation (m) for longitudinal (a, b) and lateral (c, d) velocity components. The coloured lines refer to different hours during the whole analyzed night. The horizontal error bars represent the 95% confidence bounds of the fitted spectral exponents. The vertical black dotted lines indicate the theoretical value of spectral exponents for the original signals and TA ($n = 5/3$ and $m = 4/3$, respectively)

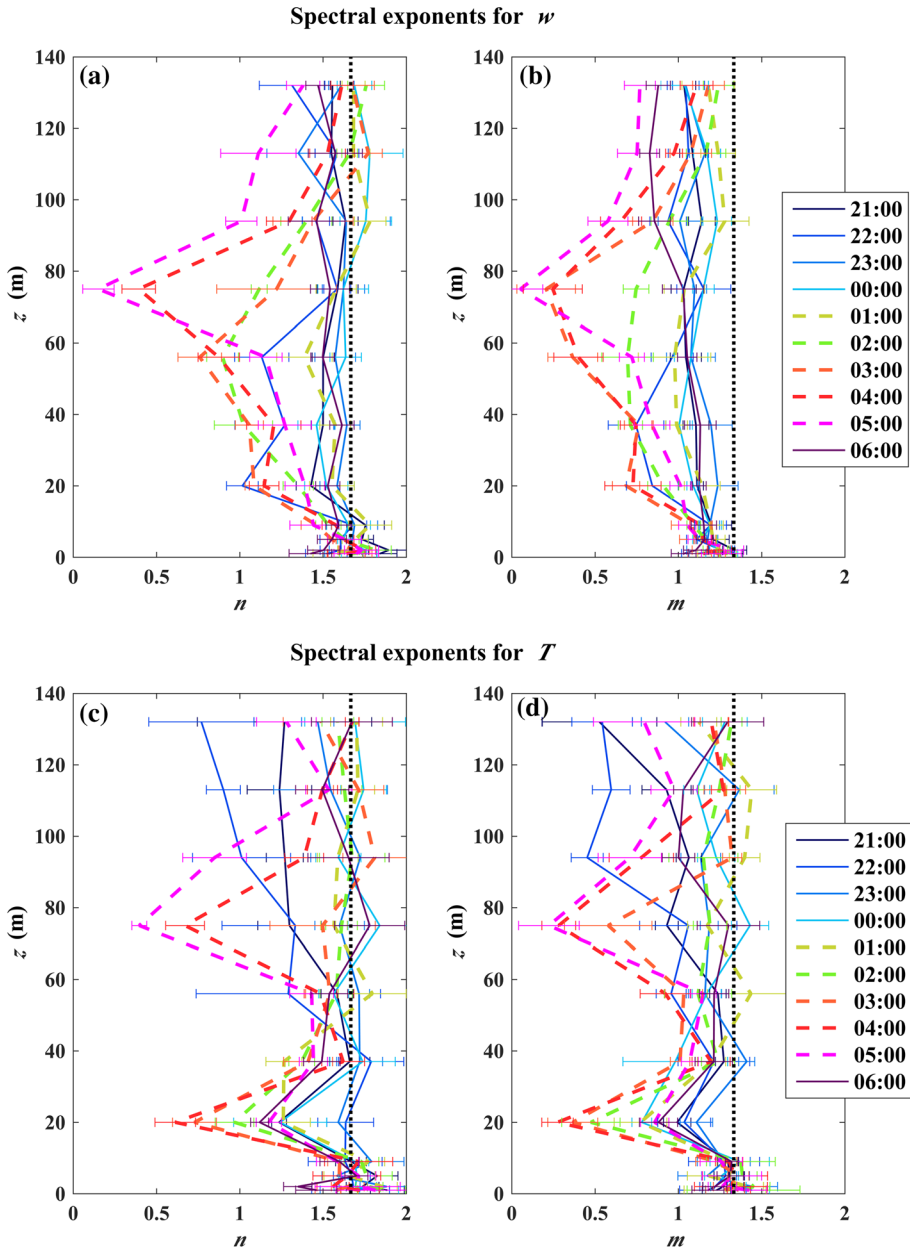


Fig. 4 Same as Fig. 3 but for vertical velocity component (a, b) and temperature (c, d)

LLJ development has been checked. Exponents appear to be linearly related before the LLJ formation (Fig. 5a) and the obtained statistical fit to the data here is consistent with the relation proposed by SB06 for fully-developed turbulence far away from boundaries (i.e. $m = (n + 1)/2$). After the LLJ development (Fig. 5b), the two spectral exponents in the SBL ($z < 20$ m) still abide by a relation similar to that proposed by SB06. On the other

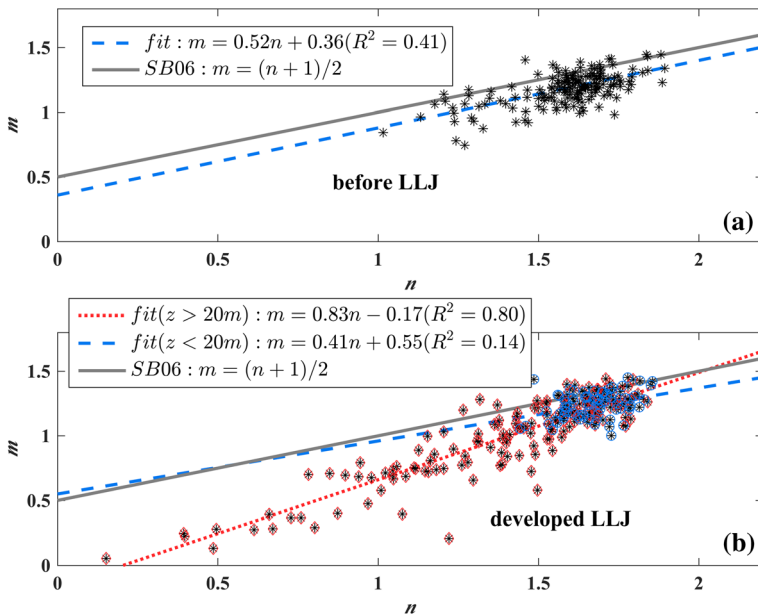


Fig. 5 Scatterplot of the spectral exponents (n) of individual 1-h runs and of their TA value (m) for all measured flow variables for the period before (a), and after (b) the LLJ development. In (a), the blue dashed line refers to the linear fit computed considering all the measurement levels. In (b), blue dashed line refers to the linear fit in the turbulent boundary layer close to the ground ($z < 20$ m; blue symbols) whereas the red dotted line refers to the linear fit above the boundary layer, that is the region dominated by submeso motions ($z > 20$ m; red symbols). As a reference, the relation proposed by SB06 (grey continuous line) is shown in both panels

hand, the relation between these two exponents deviates from $m = (n + 1)/2$ in the quiescent layer where turbulence is almost totally absent (see also Figs. 3, 4). The spectral exponents for the flow variables and their telegraphic approximation follow a linear relation (Eq. 2), but with coefficients ($a = 0.83$; $b = -0.17$) that significantly differ from those obtained by SB06.

4.2 Non-Gaussianity

An inquiry into whether the telegraphic-approximation technique preserved non-Gaussian properties of the original time series before and after LLJ development is now considered. Figure 6 shows the scatterplot of the skewness of 1-h runs (Sk) against the fraction of time when $TA(s) = 1$ (Γ_+) for all flow variables and for the period before the LLJ (Fig. 6a) and after its development (Fig. 6b). A linear relation between measured Γ_+ (determined from the TA series) and the measured skewness Sk (determined from the original time series) is noted. The obtained linear relation also agrees with the analytical relation (Eq. 4) derived from the third-order cumulant expansion not only for the period before the LLJ, but also after the LLJ developed and also in the region dominated by submeso motions (above 20 m; red symbols in Fig. 6b). This result illustrates that the telegraphic approximation captures flow features related to non-Gaussianity not only in the weakly stable boundary layer dominated by turbulent motions at the beginning of the night (non-Gaussianity

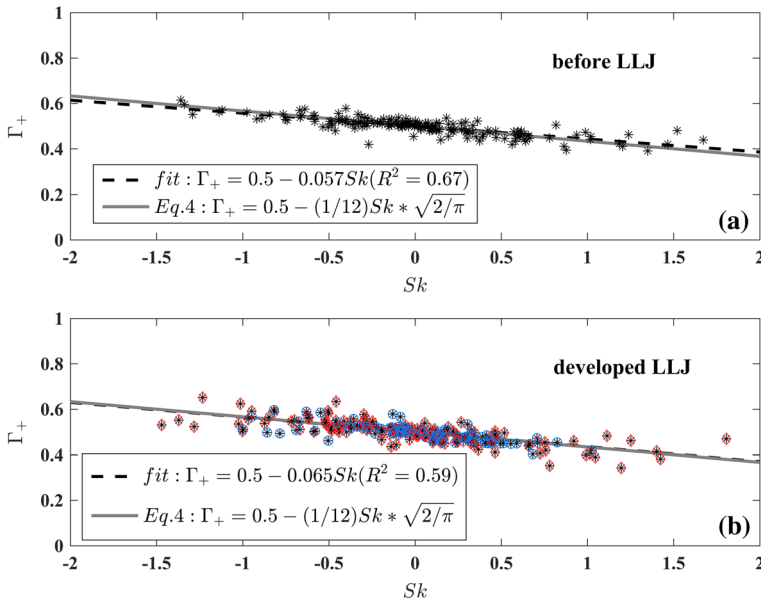


Fig. 6 Scatterplot of the skewness of individual 1-h runs (Sk) against the fraction of time $TA(s) = 1(\Gamma_+)$, for all measured flow variables for the period before, (a) and after (b) the LLJ development. The black dashed lines refer to the linear regression fits; continuous lines refer to the relationship derived using a third-order cumulant expansion (Eq. 4). In (b) blue symbols refer to data in the turbulent boundary layer close to the ground ($z < 20$ m: blue symbols) whereas the red symbols refer to data above the boundary layer, that is the region dominated by submeso motions ($z > 20$ m: red symbols)

encoded in the internal intermittency), but also in the period dominated by the LLJ and in the quiescent layer (non-Gaussianity encoded in the external intermittency). This period is characterized by the dominance of submeso motions and by quasi-complete absence of turbulence in the quiescent layer, punctuated by bursts of intermittent turbulence externally forced by nonstationarity and localized shear produced by the LLJ and submeso motions.

4.3 Clustering

Figures 7 and 8 show the evolution of the standard deviation of the running zero-crossing density fluctuations ($\overline{\delta n_\tau^2}^{1/2}$) profile for the longitudinal and vertical velocity components for the period 2100–2200 LST (before the development of the LLJ) and for the period 0400–0500 LST (developed LLJ). Before the inception of the LLJ, $\overline{\delta n_\tau^2}^{1/2}$ exhibits a behaviour that is in agreement with the overall picture presented by SB06 (Figs. 7a, c, 8a, c). As already noted in other studies (SB06; Cava and Katul 2009; Cava et al. 2012), the clustering exponents approach the value expected for a white-noise process ($\alpha \approx 0.5$) at the larger scales, whereas increased clustering occurred at the finer scales ($\alpha \approx 0.2 - 0.3$). On the other hand, a different behaviour of $\overline{\delta n_\tau^2}^{1/2}$ is evident after the LLJ developed (Figs. 7b, d, 8b, d) within the quiescent layer (coloured dashed lines in Figs. 7d, 8d). In particular, α tends to decrease (indicating an increment of clustering) approaching the value predicted by SB06 for turbulence away from boundaries at large Reynolds number ($\alpha \approx 0.1$). This behaviour can be observed not only at finer scales,

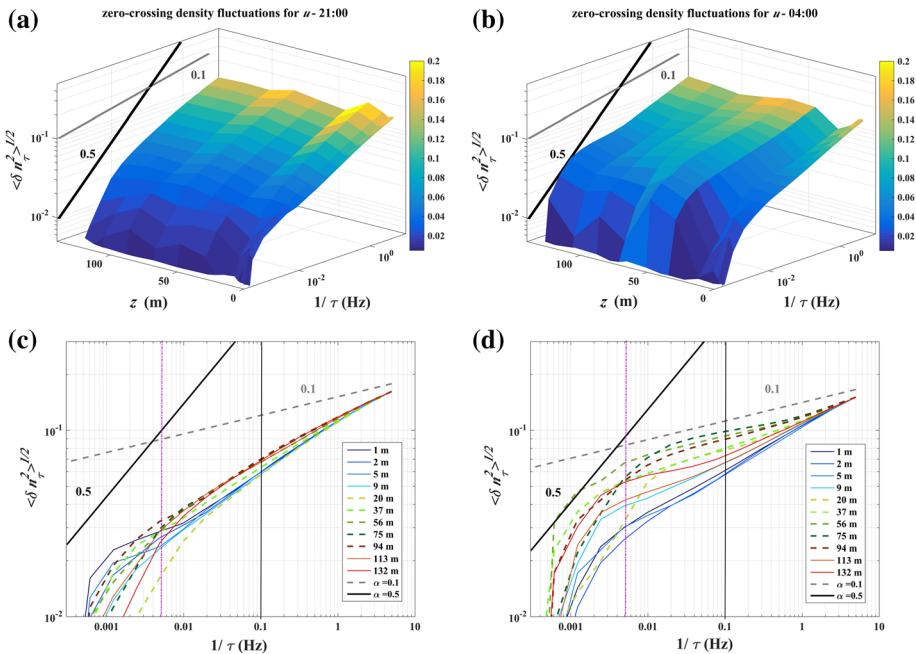


Fig. 7 3D plot of the evolution of the vertical profile of the standard deviation for the running zero-crossing density fluctuations of the longitudinal velocity (u) relative to the period 2100–2200 LST of 8 October 2016 (before the development of the LLJ) (a) and to 0400–0500 LST of 9 October 2016 (developed LLJ) (b). (c, d) The 2D version of (a) and (b), respectively, where the different colours refer to different measurement levels. As a reference, the values for white noise ($\alpha = 0.5$: black lines) and for $Re \rightarrow \infty$ ($\alpha = 0.1$: grey lines) derived from laboratory measurements by SB06 are also shown. The vertical lines delimit the ranges of frequencies used to fit the clustering exponents in the inertial subrange (ISR: 0.1 Hz–5 Hz) and in the low frequency range (LFR: 0.005 Hz–0.1 Hz)

but also at scales larger than those associated with the ISR. It is indicative of a high degree of clusterization probably related to the influence of both horizontal meandering and gravity waves that dominate the flow dynamics in the quiescent layer after LLJ development.

The hourly profiles of clustering exponents confirm the increased clusterization after the LLJ development (Figs. 9, 10). Clustering exponents for all the measured variables have been computed both in the ISR ($1/\tau > 0.1$ Hz) and in a low-frequency range (LFR: $0.005 \text{ Hz} < 1/\tau < 0.1 \text{ Hz}$). These ranges of scales have been identified on the basis of the spectral behaviour of the flow variables (see, as example, Figs. S2 and S3 in Online Resource 1). The suitability of the LFR was verified by checking the sensitivity of the fitted exponents to different choices of the low frequency limit ($f_t = 0.001 \text{ Hz}$ (LF1) – 0.002 Hz (LF2) – 0.003 Hz (LF3) – 0.01 Hz (LF4)) shown in Fig. S4 (in Online Resource 1). The clustering exponents obtained in these different ranges were compared in Fig. S5 with the values obtained in the chosen LFR ($f_t = 0.005 \text{ Hz}$). Figure S5 (in Online Resource 1) shows a good correlation for the values fitted in LF3 and LF4, when compared with the LFR (blue and red symbols and lines), confirmed also by high values of the coefficient of determination (R^2). When the LFR limit is smaller than $f_t = 0.003 \text{ Hz}$, the correlation tends to decrease but remains significant.

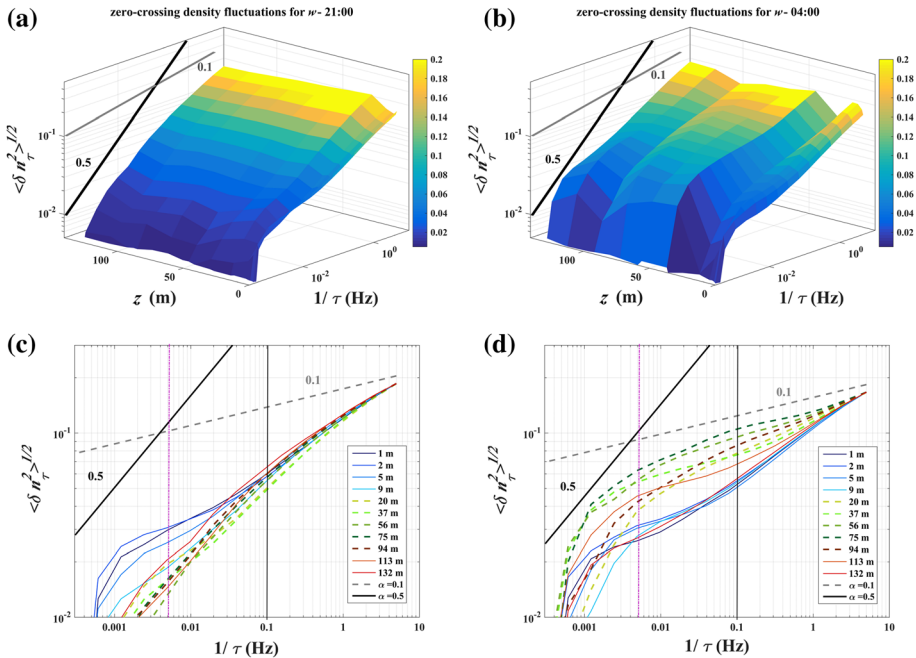


Fig. 8 Same as Fig. 7, but for the vertical velocity component

Summarizing, the performed sensitivity analysis highlights the robustness of the LFR chosen to investigate the effect of LLJ and submeso motions on clusterization and intermittency at scales larger than the ISR.

Before the LLJ development (until midnight), the clustering exponents of all the variables remain almost constant in the ISR at all measurement levels, and ranges between 0.2 and 0.3 (Figs. 9b, d, 10b, d). After 0100 LST (fully-developed LLJ) α maintains the same values in the layer close to the ground ($z < 20$ m) and in the upper turbulent layer ($z > 94$ m), whereas it decreases in the quiescent layer, often assuming values smaller than 0.2, in particular for the velocity components.

The influence of the LLJ is clear in the profiles of clustering exponents computed in the LFR (Figs. 9a, c, 10a, c). As a matter of fact, whereas before 0100 LST α assumes values ranging between 0.3 and 0.4 (closer to the white-noise value $\alpha \approx 0.5$), it dramatically drops at all the measurement levels after 0100 LST (indicating a high tendency to cluster); this reduction is observed both for the velocity components and air temperature. It is to be noted that after the development of the LLJ, α computed in the LFR often approaches the value $\alpha = 0.1$ predicted by SB06. Although the clustering exponents fitted in the LFR are affected by larger uncertainty when compared to those computed in the ISR, the obtained results indicate that submeso motions dominating the flow after the LLJ development produce an increased clusterization both at larger scales and at scales commensurate with the ISR.

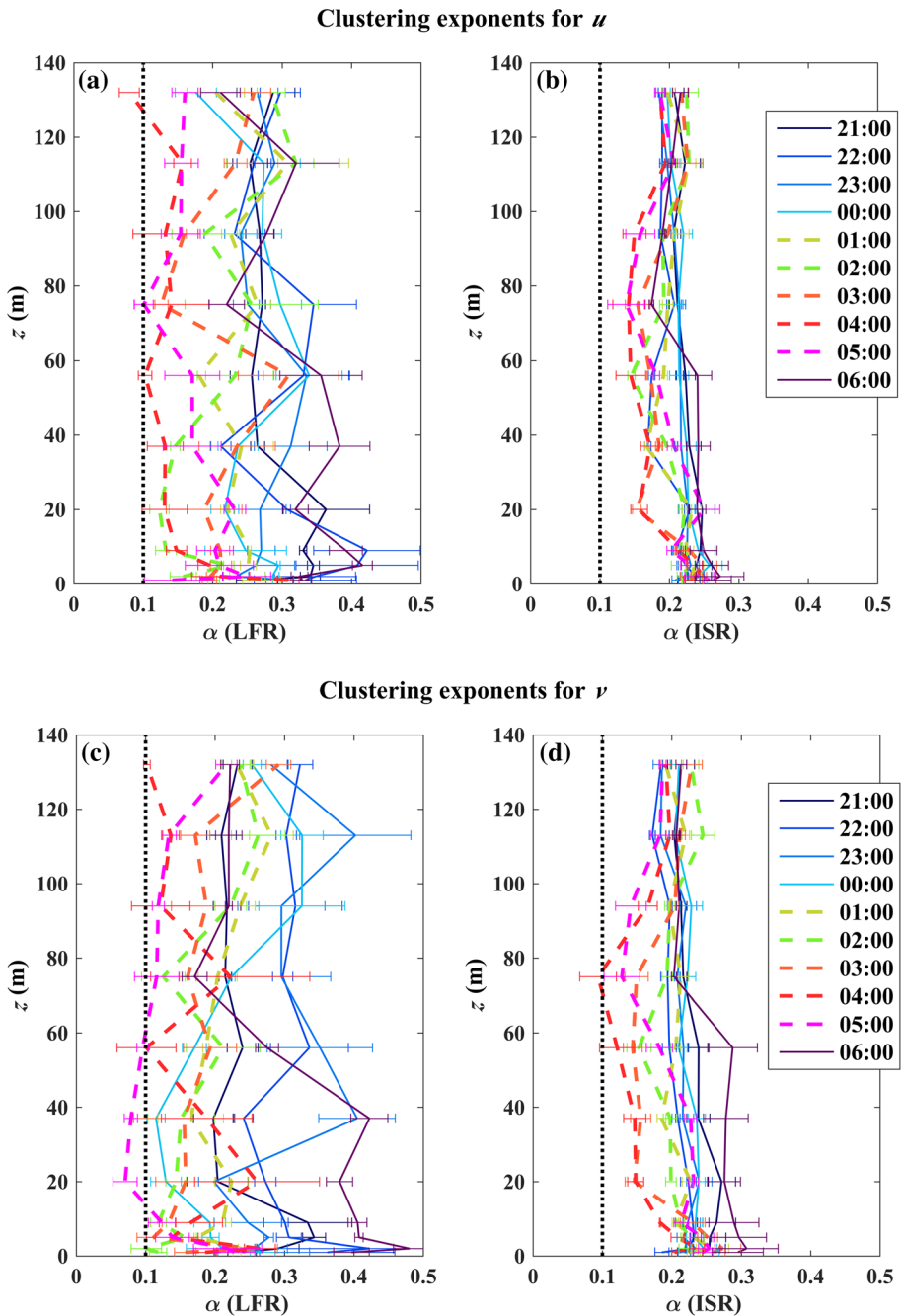


Fig. 9 Hourly vertical profiles of clustering exponents (α) computed in the low-frequency range (LFR) and in the inertial subrange (ISR) for longitudinal (**a, b**) and lateral (**c, d**) velocity components. The coloured lines refer to different hours during the whole analyzed night. The horizontal error bars represent the 95% confidence bounds of the fitted clustering exponents. The vertical black dotted lines indicate the value of α ($=0.1$) predicted by SB06 for turbulence away from boundaries that indicates a high degree of clusterization

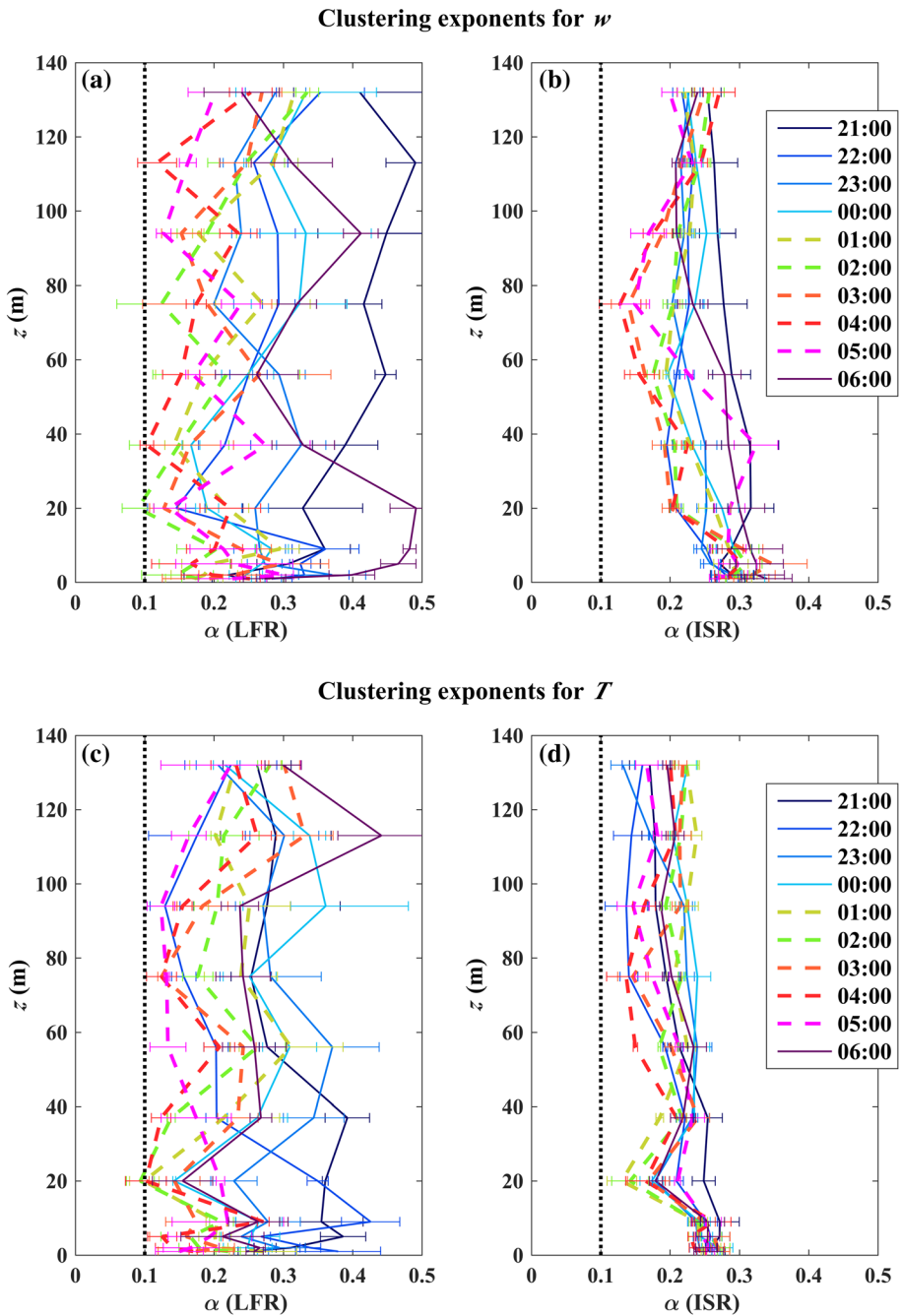


Fig. 10 Same as Fig. 9 but for the vertical velocity component (a, b) and temperature (c, d)

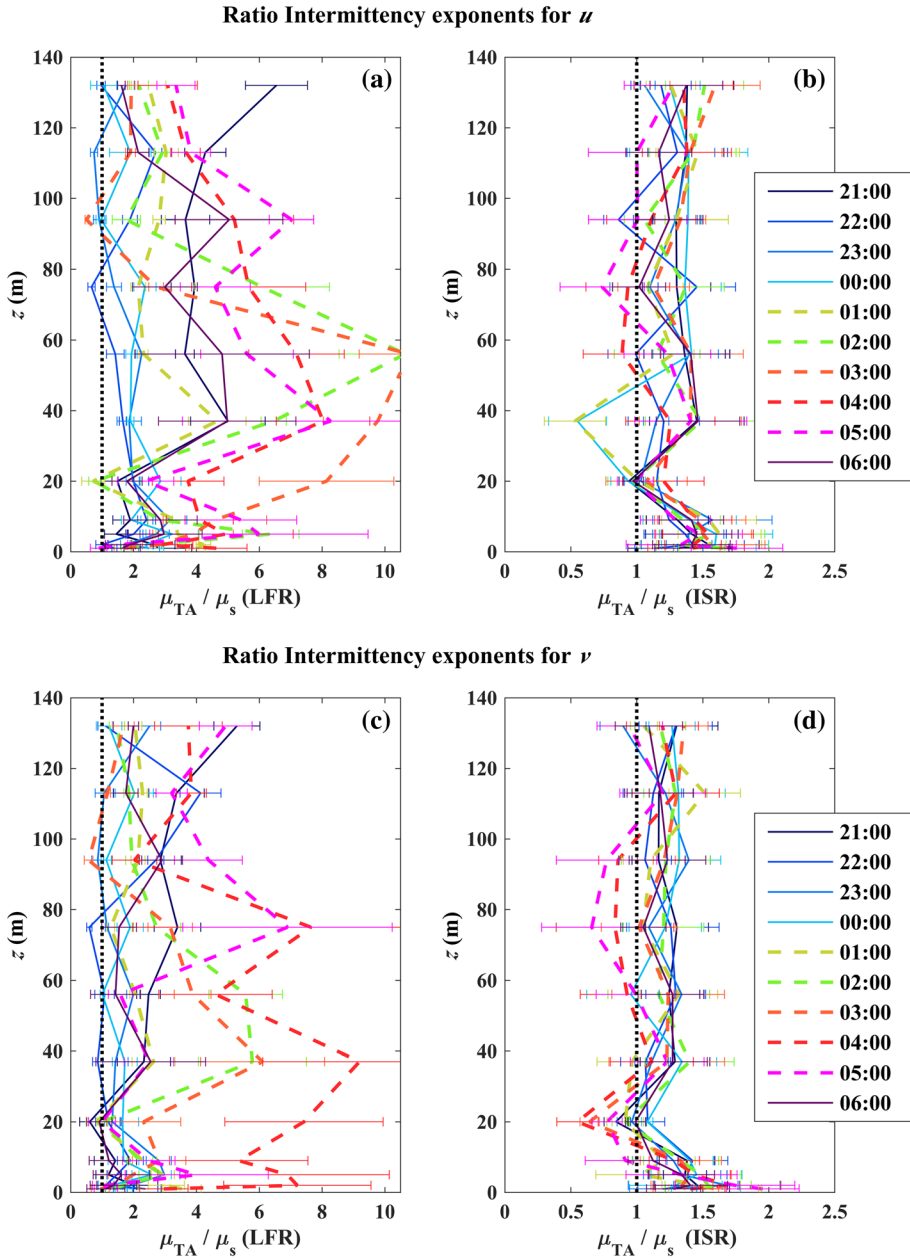


Fig. 11 Hourly vertical profiles of the ratio of intermittency exponents (μ_{TA}/μ_s) computed in the low-frequency range (LFR) and in the inertial subrange (ISR) for longitudinal (a, b) and lateral (c, d) velocity components. The coloured lines refer to different hours during the whole analyzed night. The horizontal error bars represent the error associated to the ratio of fitted intermittency exponents. The vertical black dotted lines indicate $\mu_{TA} = \mu_s$

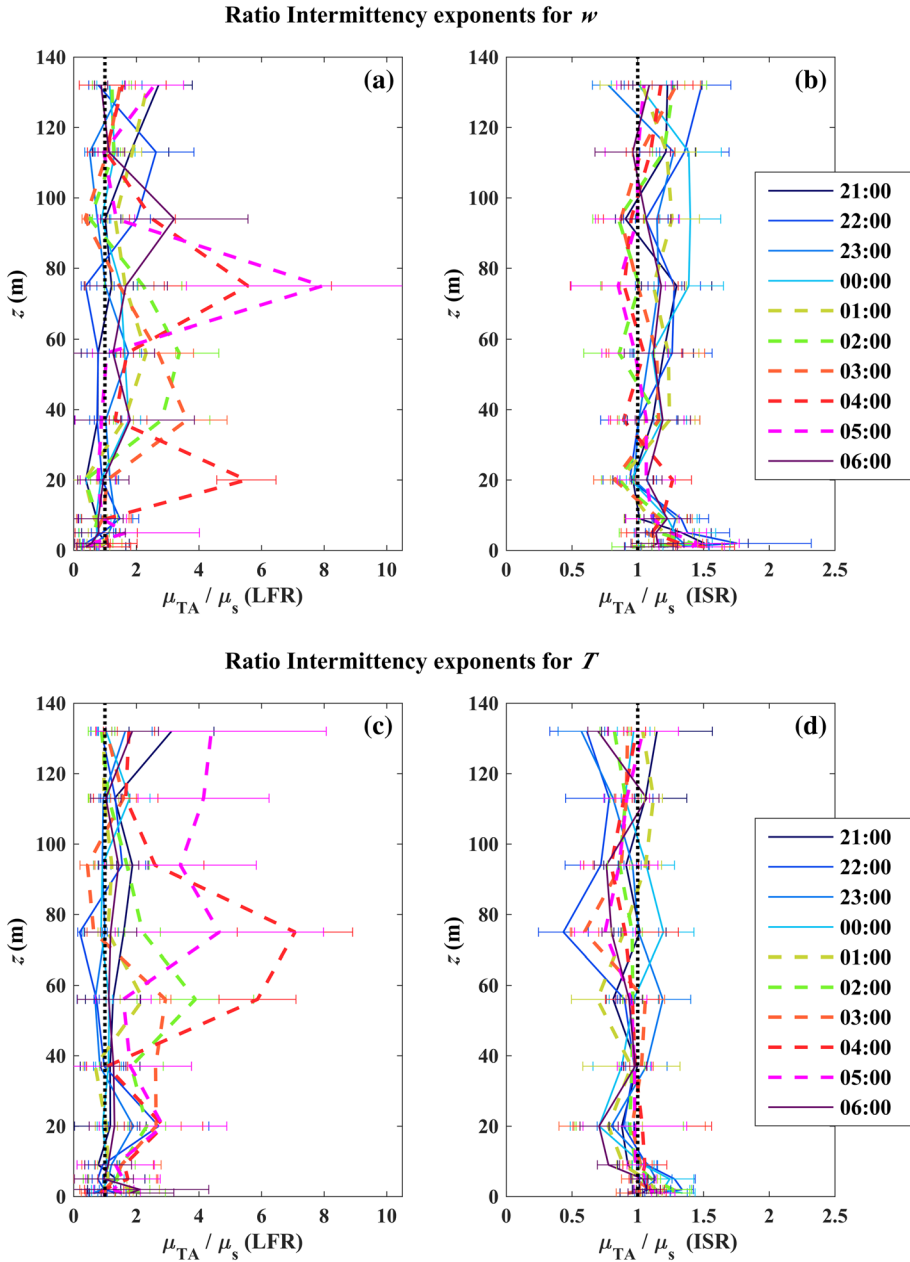


Fig. 12 Same as Fig. 11 but for the vertical velocity component (a, b) and temperature (c, d)

4.4 Intermittency Exponents

Figures 11 and 12 show the hourly profiles of the intermittency exponent ratio (μ_{TA}/μ_s) for the measured variables during the entire evening. Analogous to clustering exponents,

the intermittency exponents for the original series (μ_s) and its telegraphic approximation (μ_{TA}) have been computed both in the ISR and in the low-frequency ranges. The sensitivity analysis for the fitted intermittency exponents in the different low-frequency ranges (Figs. S6 and S7 in Online Resource 1) confirm that the results obtained for clustering exponents are robust. At the finer scales, the ratio of intermittency exponents does not greatly vary during the night across the measurement levels (Figs. 11b, d, 12b, d). For the velocity components, this ratio exceeds unity ($\mu_{TA} > \mu_s$) mainly before the LLJ development, indicating a tendency for amplitude fluctuations to mitigate the effect of intermittency for those variables. On the other hand, the ratio is about unity ($\mu_{TA} \approx \mu_s$) for temperature suggesting that intermittency is prevalently related to clustered structures for this flow variable in the ISR.

Before the development of the LLJ, the ratio (μ_{TA}/μ_s) in the LFR exceeds unity for the u component and is about unity for w and T (Figs. 11a, c, 12a, c). Interestingly, the ratio significantly increases in the LFR after the LLJ development, implying that intermittency is primarily driven by clusterization. This behaviour is mainly observed at levels close to the LLJ nose ($z = 56$ m) for w and T (Fig. 12a, c), whereas it is evident

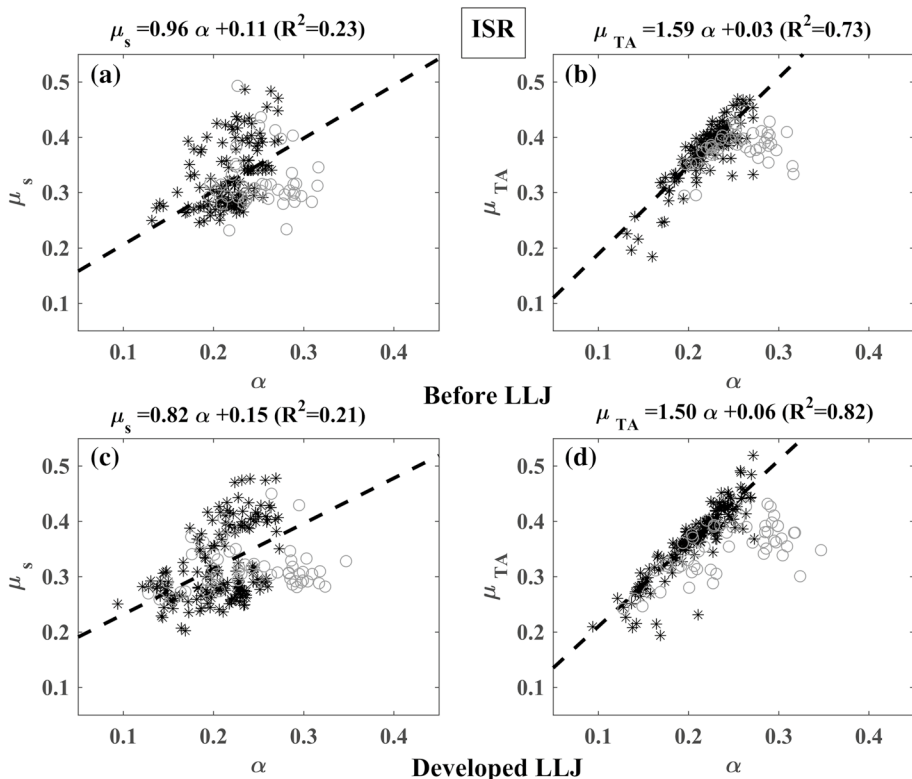


Fig. 13 Scatterplot of the global intermittency exponents (μ_s) and of the TA intermittency exponents (μ_{TA}) versus the clustering exponents (α) relative to the inertial subrange (ISR) for the period before (a, b) and after (c, d) the LLJ development. The dashed lines refer to the linear regression fits relative to the variables ($s = u, v, T$; black stars); grey circles refer to the same quantities for the vertical velocity component (w)

across all measurement levels for the horizontal velocity components, suggesting that horizontal meandering may be driving this process (Fig. 11a, c).

Figure 13 shows the relation between the hourly clustering exponent α and the hourly global and TA intermittency exponents (μ_s , μ_{TA}) computed in the ISR before and after the development of the LLJ. In spite of the scatter, the investigated quantities computed for u , v , T (black symbols) exhibit a linear correlation, and of particular significance here is the relation between μ_{TA} and α . The regression slopes and intercepts ($\mu_s = a'\alpha + b'$; $\mu_{TA} = a''\alpha + b''$) do not vary appreciably for hours before and after the development of the LLJ. The mean regressions computed considering the whole nocturnal period are $\mu_s = 0.87\alpha + 0.14$ ($R^2 = 0.22$); $\mu_{TA} = 1.50\alpha + 0.05$ ($R^2 = 0.77$) and agree with regressions found at sites characterized by various values of aerodynamic roughness length (Cava et al. 2012). Moreover, the same quantities computed for the vertical velocity component (grey symbols in Fig. 13) appear de-correlated, as already found in Cava et al. (2012). The aforementioned study observed an increased de-correlation with progressively increasing smoothness of the surface, as a consequence of the roughness impact on the structure of fine-scale turbulence.

The same relations have been checked for exponents estimated in the LFR (Fig. 14). As expected, a more discernible linear relation is evident after the development of the LLJ (Fig. 14c, d) because the presence of submeso motions produces an increased clusterization in this range of scales (absent before the LLJ development). The linear

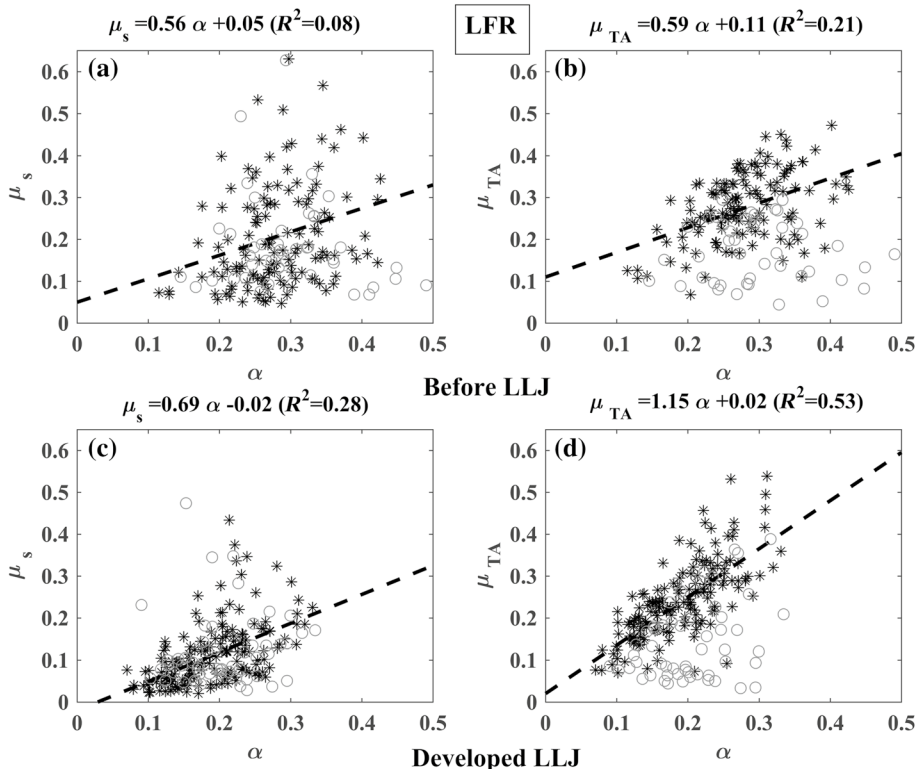


Fig. 14 Same as Fig. 13 but for exponents relative to the low frequency range (LFR)

correlation obtained after the development of the LLJ is more significant for μ_{TA} versus α ($\mu_s = 0.69 - 0.02(R^2 = 0.28)$; $\mu_{TA} = 1.15\alpha + 0.02(R^2 = 0.53)$), analogous to that obtained at ISR scales, even if characterized by a large scatter. Moreover, the investigated quantities appear decorrelated for w in the LFR.

4.5 Interpulse Periods

The probability density functions $p(I_p)$ of the interpulse period I_p relative to the period 2100–2200 LST (before the development of the LLJ) and to 0300–0400 LST (developed LLJ) for all the measured variables are shown in Fig. S8 (in Online Resource 1). These functions appear to be well described by a power-law distribution ($p(I_p) \sim I_p^{-\gamma}$), mainly for short interpulse periods, both before the LLJ (top panels of Fig. S8) and after the full development of the LLJ (bottom panels of Fig. S8). This behaviour is observed both in the stable boundary layer ($z < 20$ m: blue symbols) and above ($z > 20$ m: red symbols). The exponents (γ) of the power-law fits have been estimated and the linkages with spectral and intermittency exponents have been checked. Figure 15 shows the scatterplot of the modelled versus measured hourly spectral exponents of the telegraphic approximation of all the flow variables and for the period before and after the LLJ development. The relation proposed for a weighted superposition of Poisson processes and for some classical models of self-organized criticality has been checked (Eq. 7: $m = 3 - \gamma$ —circles and dotted lines in Fig. 15), as well as the correction for intermittency effect (Eq. 8: $m = 3 - \gamma - \mu_s/2$ —stars

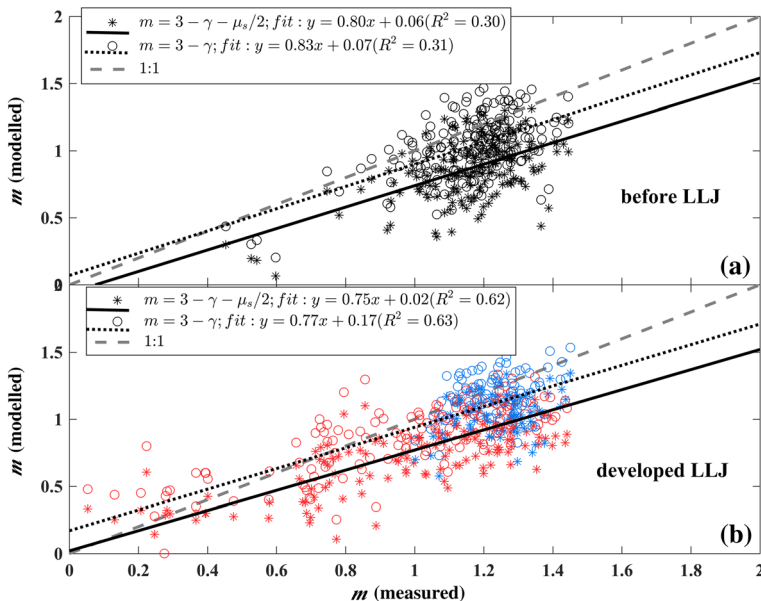


Fig. 15 Scatterplot of the modelled versus measured hourly spectral exponents of TA for all flow variables and for the period before (a) and after (b) the LLJ development. The black continuous and dotted lines refer to the linear regression fits relative to the two models. As a reference the 1:1 line is reported (grey dashed line). In fig. b blue symbols refer to data in the turbulent boundary layer close to the ground ($z < 20$ m: blue symbols) whereas the red symbols refer to data above the boundary layer, that is the region dominated by submeso motions ($z > 20$ m: red symbols)

and continuous lines in Fig. 15). The obtained linear fits highlight that the two models are acceptable before and after the LLJ development across all measurement levels. Moreover, because the additional intermittency correction does not produce any improvements, the SOC relation $m = 3 - \gamma$ seems to be a reasonable model both in the thin stable layer close to the ground ($z < 20$ m: blue symbols in Fig. 15b) and in the quiescent layer ($z > 20$ m: red symbols in Fig. 15b) dominated by submeso motions after the development of the LLJ. This finding suggests a negligible role of small-scale intermittency in this setting where clustering and large-scale intermittency are the dominant mechanisms.

5 Conclusions

Multi-level high-frequency wind-velocity time series were analyzed using measurements from a tall (= 140 m) meteorological tower. The analysis seeks to explore transitions from a mildly stable boundary layer characterized by fully-developed turbulence to one dominated by a low-level jet (LLJ) and quiescent layers with weak or intermittent turbulence often detached from the ground. The telegraphic approximation was applied to investigate analogies to a general class of intermittency models in terms of clustering properties of sign changes of the flow variables for describing switching between turbulent (active) and non-turbulent (passive) states in the very stable boundary layer.

The telegraphic-approximation technique captured the main feature of the flow related to the spectral properties and to non-Gaussianity even in non-turbulent situations. That is, the telegraphic approximation provided a new perspective on clustering and intermittency (external and internal) for periods and for layers dominated by, (i) turbulent motions, (ii) LLJ propagation and submeso motions, and (iii) for periods with quasi-complete absence of turbulence punctuated by bursts of intermittent turbulent energy externally forced by non-stationary and localized shear produced by LLJ and submeso motions. The observed behaviour in clustering and intermittency exponents indicate that the submeso motions were highly clustered and their influence produced an increased intermittency both at larger scales and at finer scales commensurate with the ISR, mainly driven by clusterization. The analysis here provided evidence of a self-organized-criticality (SOC) like behaviour between switching probability of active–inactive states (linked to m , the spectral exponents for TA) and lifetimes of inactive states (linked to γ , the exponent of the power-law distribution of interpulse periods). The SOC relation $m = 3 - \gamma$, originally derived for sand-pile models near critical states (i.e. avalanches) (Bak et al. 1988), was shown to be applicable to all layers in the SBL. These layers include the thin stable boundary layer close to the ground characterized by fully-developed turbulence, the quiescent layer, and layers dominated by the LLJ. The implications here are that SBL flows can be associated with a single SOC process with a tuning parameter related to Ri . In the analyzed dataset here, $Ri \approx [0.1, 0.25]$ persisted near the ground for almost all the evening after the LLJ formation and may be viewed as an outcome of self-tuning around a second-order phase transition from fully-developed turbulence ($Ri < 0.25$) to one dominated by submeso motions in the quiescent layer ($Ri \approx [0.25, 0.5]$). When $Ri < 0.25$, hallmarks of both SOC and fully-developed turbulence (including in the jet and the shallow region near the ground) coexistence were evident. Self-organized criticality signatures appeared in the form of power-law avalanche statistics captured by $p(I_p) \sim I_p^{-\gamma}$, whereas turbulence signatures were captured by conventional spectra, intermittency, and clustering exponents. When $Ri > 0.25$, the turbulence signatures were no longer present but SOC signatures persisted within the quiescent

layer (at least as captured by its telegraphic state). In the quiescent layer both enhanced energy and increased clustering at low frequency seem to be consistent with meandering and submeso motions that developed after the formation of the LLJ.

It must be emphasized that the analogy to SOC here is only diagnostic (not prognostic) and applies to the telegraphic-approximation properties of the SBL (turbulent and non-turbulent). However, the results encourage further studies to confirm coexistence of self-organized criticality and intermittent turbulence in the SBL and to propose innovative scaling laws and similarity arguments that may improve performances of numerical weather prediction and dispersion models in stable atmosphere, at least in terms of intermittency and on–off switching.

Acknowledgements The study has been developed within the context of a Research and Development project sponsored by companies Linhares Geração S.A. and Termelétrica Viana S.A., and named “Desenvolvimento de um modelo operacional para simulação em tempo real da dispersão atmosférica de poluentes emitidos por termelétrica a gás natural”. The Project is within the context of the investment program in Research and Development, regulated by Brazilian National Agency for Electric Energy. G.Katul acknowledges partial support from the U.S. National Science Foundation (NSF-EAR-1344703, NSF-AGS-1644382, and NSF-DGE-1068871). We would like to also acknowledge the collaboration with the Marche Region, and in particular the “Environmental assessments and authorizations, air quality and natural protection” section.


References

- Acevedo OC, Mahrt L, Puhales FS, Costa FD, Medeiros LE, Degrazia GA (2015) Contrasting structures between the decoupled and coupled states of the stable boundary layer. *Q J R Meteorol Soc* 142:693–702. <https://doi.org/10.1002/qj.2693>
- Acevedo OC, Degrazia GA, Puhales FS, Martins LGN, Oliveira PES, Teichrieb C, Silva SM, Maroneze R, Bodmann B, Mortarini L, Cava D, Anfossi D (2018) Monitoring the micrometeorology of a coastal site next to a thermal power plant from the surface to 140 m. *Bull Am Meteorol Soc* 99(4):725–738. <https://doi.org/10.1175/BAMS-D-17-0134.1>
- Bak P, Tang C, Wiesenfeld K (1988) Self-organised criticality. *Phys Rev A* 38:364–374. <https://doi.org/10.1103/PhysRevA.38.364>
- Banta RM, Mahrt L, Vickers D, Sun J, Balsley BB, Pichugina YL, Williams EJ (2007) The very stable boundary layer on nights with weak low-level jets. *J Atmos Sci* 64:3068–3090. <https://doi.org/10.1175/JAS4002.1>
- Bershadskii A, Niemela JJ, Praskovsky A, Sreenivasan KR (2004) Clusterization and intermittency of temperature fluctuations in turbulent convection. *Phys Rev E* 69:056314. <https://doi.org/10.1103/PhysRevE.69.056314>
- Bou-Zeid E, Gao X, Anson C, Katul GG (2018) On the role of return to isotropy in wall-bounded turbulent flows with buoyancy. *J Fluid Mech* 856:61–78. <https://doi.org/10.1017/jfm.2018.693>
- Cava D, Katul GG (2009) The effects of thermal stratification on clustering properties of canopy turbulence. *Boundary-Layer Meteorol* 130:307–325. <https://doi.org/10.1007/s10546-008-9342-6>
- Cava D, Katul GG, Molini A, Elefante C (2012) The role of surface characteristics on zero-crossing properties of atmospheric turbulence. *J Geophys Res* 117:D01104. <https://doi.org/10.1029/2011JD016167>
- Giostra U, Cava D, Schipa S (2002) Structure functions in a wall-turbulent shear flow. *Boundary-Layer Meteorol* 103:337–359. <https://doi.org/10.1023/A:1014917120110>
- Grachev AA, Fairall CW, Persson POG, Andreas EL, Guest PS (2005) Stable boundary-layer scaling regimes: the SHEBA data. *Boundary-Layer Meteorol* 116:201–235. <https://doi.org/10.1007/s10546-004-2729-0>
- Jensen HJ (1998) Self-organised Criticality. Cambridge University Press, Cambridge
- Katul GG (1994) A model for sensible heat flux probability density function for near-neutral and slightly stable atmospheric flows. *Boundary-Layer Meteorol* 71:1–20. <https://doi.org/10.1007/BF00709217>
- Katul GG, Parlange MB, Chu CR (1994) Intermittency, local isotropy, and non-Gaussian statistics in atmospheric surface-layer turbulence. *Phys Fluids* 6(7):2480–2492. <https://doi.org/10.1063/1.868196>

- Katul GG, Hsieh CI, Kuhn G, Ellsworth D, Nie DL (1997) Turbulent eddy motion at the forest–atmosphere interface. *J Geophys Res* 102:13409–13421. <https://doi.org/10.1029/97JD00777>
- Katul GG, Vidakovic B, Albertson J (2001) Estimating global and local scaling exponents in turbulent flows using discrete wavelet transformations. *Phys Fluids* 13:241–250. <https://doi.org/10.1063/1.1324706>
- Katul GG, Poggi D, Cava D, Finnigan J (2006) The relative importance of ejections and sweeps to momentum transfer in the atmospheric boundary layer. *Boundary-Layer Meteorol* 120:367–375. <https://doi.org/10.1007/s10546-006-9064-6>
- Katul GG, Porporato A, Poggi D (2009) Roughness effects on fine-scale anisotropy and anomalous scaling in atmospheric flows. *Phys Fluids* 21:035106. <https://doi.org/10.1063/1.3097005>
- Kolmogorov AN (1941) The local structure of turbulence in incompressible viscous fluid for very large Reynolds number. *Dokl Akad Nauk SSSR* 30:9–13
- Kuznetsov E, Newell AC, Zakharov VE (1991) Intermittency and turbulence. *Phys Rev Lett* 67:3243–3246. <https://doi.org/10.1103/PhysRevLett.67.3243>
- Kuznetsov VR, Praskovsky AA, Sabelnikov VA (1992) Fine scale turbulence structure of intermittent shear flows. *J Fluid Mech* 243:595–622. <https://doi.org/10.1017/S0022112092002842>
- Lan C, Liu H, Li D, Katul GG, Finn D (2018) Distinct turbulence structures in stably stratified boundary layers with weak and strong surface shear. *Atmospheres, J Geophys Res*. <https://doi.org/10.1029/2018JD028628>
- Mahrt L (1998) Stratified atmospheric boundary layers and breakdown of models. *Theor Comput Fluid Dyn* 11:263–279. <https://doi.org/10.1007/s001620050093>
- Mahrt L (2014) Stably stratified atmospheric boundary layers. *Annu Rev Fluid Mech* 46:23–45. <https://doi.org/10.1146/annurev-fluid-010313-141354>
- Meneveau C (1991) Analysis of turbulence in the orthonormal wavelet representation. *J Fluid Mech* 232:469–520. <https://doi.org/10.1017/S0022112091003786>
- Molini A, Katul GG, Porporato A (2009) Revisiting rainfall clustering and intermittency across different climatic regimes. *Water Resour Res* 45(11):W11403. <https://doi.org/10.1029/2008WR007352>
- Monahan AH, Rees T, He Y (2015) Multiple regimes of wind, stratification, and turbulence in the stable boundary layer. *J Atmos Sci* 72:3178–3198. <https://doi.org/10.1175/JAS-D-14-0311.1>
- Mortarini L, Cava D, Giostra U, Acevedo O, Nogueira Martins LG, Soares de Oliveira PE, Anfossi D (2018) Observations of submeso motions and intermittent turbulent mixing across a low level jet with a 132-m tower. *Q J R Meteorol Soc* 144:172–183. <https://doi.org/10.1002/qj.3192>
- Nakagawa H, Nezu I (1977) Prediction of contributions to Reynolds stress from bursting events in open-channel flows. *J Fluid Mech* 80:99–128. <https://doi.org/10.1017/S0022112077001554>
- Obukhov AM (1962) Some specific features of atmospheric turbulence. *J Geophys Res* 67:3011–3014. <https://doi.org/10.1029/JZ067i008p03011>
- Pahlow M, Parlange MB, Porté-Agel F (2001) On Monin–Obukhov similarity theory in the stable atmospheric boundary layer. *Boundary-Layer Meteorol* 99:225–248. <https://doi.org/10.1023/A:1018909000098>
- Poggi D, Katul GG (2009) Flume experiments on intermittency and zero-crossing properties of canopy turbulence. *Phys Fluids* 21:065103. <https://doi.org/10.1063/1.3140032>
- Poggi D, Porporato A, Ridolfi K (2003) Analysis of the small-scale structure of turbulence on smooth and rough walls. *Phys Fluids* 15:35. <https://doi.org/10.1063/1.1521728>
- Poggi D, Katul GG, Albertson JD (2004) Momentum transfer and turbulent kinetic energy budgets within a dense model canopy. *Boundary-Layer Meteorol* 111:589–614. <https://doi.org/10.1023/B:BOUN.0000016502.52590.af>
- Pruessner G (2012) Self-organized criticality: theory, models, and characterization. Cambridge University Press, Cambridge
- Raupach MR (1981) Conditional statistics of Reynolds stress in rough-wall and smooth-wall turbulent boundary-layers. *J Fluid Mech* 108:363–382. <https://doi.org/10.1017/S0022112081002164>
- Salehipour H, Peltier WR, Caulfield CP (2018) Self-organized criticality of turbulence in strongly stratified mixing layer. *J Fluid Mech* 856:228–256. <https://doi.org/10.1017/jfm.2018.695>
- Shi B, Vidakovic B, Katul GG, Albertson JD (2005) Assessing the effects of atmospheric stability on the fine structure of surface layer turbulence using local and global multiscale approaches. *Phys Fluids* 17:005104. <https://doi.org/10.1063/1.1897008>
- Smyth WD, Moum JN (2000) Anisotropy of turbulence in stably stratified mixing layers. *Phys Fluids* 12:1343–1362. <https://doi.org/10.1063/1.870386>
- Sornette D (2003) Critical phenomena in natural sciences: chaos, fractals, selforganization, and disorder: concepts and tools. Springer, Berlin
- Sreenivasan KR, Antonia RA (1997) The phenomenology of small-scale turbulence. *Annu Rev Fluid Mech* 29:435–472. <https://doi.org/10.1146/annurev.fluid.29.1.435>

- Sreenivasan KR, Bershadskii A (2006) Clustering properties in turbulent signals. *J Stat Phys* 125:1145–1153. <https://doi.org/10.1007/s10955-006-9112-0>
- Sreenivasan KR, Bershadskii A, Niemela JJ (2004) Multiscale SOC in turbulent convection. *Physica A* 340(4):574–579
- Stiperski I, Calaf M (2018) Dependence of near-surface similarity scaling on the anisotropy of atmospheric turbulence. *Q J R Meteorol Soc* 144:641–657. <https://doi.org/10.1002/qj.3224>
- Tennekes H (1973) Intermittency of the small-scale structure of atmospheric turbulence. *Boundary-Layer Meteorol* 4:241–250. <https://doi.org/10.1007/BF0226523>
- Uritsky VM, Paczuski M, Davila JM, Jones SI (2007) Coexistence of self-organized criticality and intermittent turbulence in the solar corona. *Phys Rev Lett* 99(2):025001
- Vercauteren N, Boyko V, Faranda D, Stiperski I (2018) Scale interactions and anisotropy in stable boundary layers. [arXiv:1809.07031v1](https://arxiv.org/abs/1809.07031) [physics.flu-dyn]

Affiliations

Daniela Cava¹  · **Luca Mortarini**^{1,2} · **Umberto Giostra**³ · **Otavio Acevedo**² · **Gabriel Kattul**^{4,5}

¹ Institute of Atmospheric Sciences and Climate - National Research Council, Torino, Italy

² Universidade Federal de Santa Maria, Santa Maria, Brazil

³ Department of Pure and Applied Sciences (DiSPeA), Università degli Studi di Urbino “Carlo Bo”, Scientific Campus “E. Mattei”, 61029 Urbino, Italy

⁴ Nicholas School of the Environment, Duke University, P.O. Box 80328, Durham, NC 27708, USA

⁵ Department of Civil and Environmental Engineering, Duke University, Durham, NC 27708, USA